Influence of transcrystalline layer on finite element mesoscale modeling of polyamide 6 based single polymer laminate composites

Shafagh. D. Tohidi[a,b,e*], Ana Maria Rocha[a], N. Dourado[b], Mohammadali Rezazadeh[c], Nguyễn T. Quyền [a], Andrea Zille[a], Stefan Hesseler[d], Thomas Gries[d], Nadya V. Dencheva[e], Zlatan Denchev[e]

[a)] *Center of Textile Science and Technology (2C2T), Department of Textile Engineering, University of Minho, Guimarães, Portugal.*
[b)] *CMEMS-UMinho, Department of Mechanical Engineering, University of Minho, Guimarães, Portugal*
[c)] *ISISE, Department of Civil Engineering, University of Minho, Guimarães, Portugal*
[d)] *ITA, Institute für Textiltechnik of RWTH Aachen University, Aachen, Germany*
[e)] *IPC - Institute for Polymers and Composites, Department of Polymer Engineering, University of Minho, Guimarães, Portugal.*

Abstract

This study presents a novel approach for finite element modeling of the elastic behavior of a plain-woven reinforced single polymer laminate composites (WSPC) based on polyamide 6 (PA6). These composites are produced via compression molding of PA6 woven textile structures that are powder-coated by anionic PA6 microparticles. Morphological and structural analysis complemented by electron microscopy, image processing and X-ray diffraction suggest the presence of transcrystalline layer (TCL) at the matrix-reinforcement interface. Having in mid this experimental fact, a novel procedure is developed for finite level discretization of TCL in the representative volume element (RVE) during tensile straining. The procedure correlates the material properties with the overall load applied, thus adequately modelling the tensile behavior of the WSPC based on the constituent materials. The stress field along the elements of the RVE model is studied while the tensile loads were applied in two principal directions. A good agreement between the real mechanical behavior and that calculated based on the model was demonstrated.

---

[*] Address correspondence to this author at the Center of Textile Science and Technology (2C2T), Department of Textile Engineering, University of Minho, Guimarães, Portugal.; Tel: +351-918562529; E-mail: Shafagh.project@gmail.com

1. Introduction

Single-polymer composites (SPC) were introduced several decades ago by Capiati and Porter [1], in which both polymer matrix and reinforcements (i.e. filaments, fabrics and particles) are made of the same polymer. As opposed to the traditional composite materials, SPC are chemically homogeneous, which leads to strong and durable interactions across the matrix-reinforcement interface [2], distinct chemical functionality [3] and full recyclability via reprocessing [4]. There exist comprehensive reviews on the SPC preparation, morphology, and mechanical behavior [1,5,6]. Because of the identity of the matrix and the reinforcement materials in SPC, their processing window (i.e., the difference between the melting of the non-oriented matrix and the melting of the oriented reinforcements) does not exceed several degrees. Therefore, very frequently overheating and partial melting of the reinforcing elements takes place during the SPC consolidation by traditional molding techniques that irreversibly degrades the mechanical properties of the final composite [7–9]. Successful attempts were made to create SPC, predominantly based on polyamide 6 (PA6), using reactive processing techniques in which the matrix is created in-situ by anionic polymerization [10–14] thus significantly widening the processing window.

Plain-woven reinforced composites to which the above PA6-based SPC belong, are extensively used in industry due to their orthotropic nature that enables prediction/modelling of their mechanical behavior. However, only the mechanical behavior of neat textile structures or traditional heterogeneous composites have been subjected of experimental and numerical studies performing micromechanical-parametric investigation [15–17]. It is to mention that the virtual simulations of textile reinforcements are relatively complex. Effectively, to represent the configuration of filaments in textile reinforcement structures, many different forms of geometry have been put forward by textile researchers [18–22]. Furthermore, in the case of composite materials, the representative volume element (RVE) with appropriate size is to be divided into two principal sub-elements belonging to the fibrous and the matrix components, respectively [16,23]. The overall elastic property of the RVE is calculated by assembling the compliance matrix of the sub-elements under iso-stress assumption.

There exist finite element models for plain-woven reinforced composites to monitor the occurrence of internal damage at different loading levels and observe the stress field along the composite components [15,16,24]. Barbero et al. [15] developed RVE of plain-weave fabric-reinforced composites whereby the

geometrical models of sub-elements were constructed via image analysis of lamina. The authors studied the non-linear behavior of plain-weave reinforced laminates under tensile loading by applying a meso-level damage model. It was concluded that the proposed model predicts the appearance of a macrocrack at a stress level of 294 MPa, which was found in good agreement with experimental results. Potluri and Thammandra [16] presented a RVE model of plain-woven reinforced E-glass/polyester composites demonstrating the crimp interchange that results from uniaxial stress and filament flattening due to biaxial stress. Their finite element method (FEM) based micro-mechanical models were simulated based on unstrained, biaxially strained and uniaxially strained plain-woven fabric. Their results showed 19% increase on tensile modulus of RVE with biaxially strained fabrics as compared with the ones with unstrained fabric. Finally, Blackletter et al. [24] constructed a 3D finite element RVE model to describe damage propagation in a plain-woven reinforced graphite/epoxy composite material subjected to tension or shear loading. To analyze loading response, an incremental iterative finite element algorithm was developed in which its anisotropic plasticity behavior was predicted and a scheme to estimate the effects of damage propagation by stiffness reduction. Their results showed nonlinear shear stress-strain behavior which was related to the damage propagation rather than to plastic deformation of the matrix.

Generally, the stiffness and strength behavior of composites are depended upon the reinforcement architecture and material properties of filaments, matrix and their interface [25]. In SPC, the reinforcement and the matrix are made of same polymer affinity which is enhances their mechanical properties. Moreover, having in mind the preparation of the SPC that includes a consolidation step by melting and crystallization of the PA6 matrix in the presence of oriented PA6 filaments, a columnar layer of matrix material is created around the monofilaments, named transcrystalline layer (TCL). The latter has a key influence on the mechanical properties of the final composites [26]. Generally, TCL is affected by the crystallization conditions [27,28]. Other important factors influencing TCL are: the epitaxy between fiber/matrix, the topography of the fiber, the presence of mismatch between the thermal coefficients of the fiber and the matrix, the chemical composition on the fiber surface, the crystallinity of the fiber, the processing conditions and the surface roughness of fibers among others [29–32].

This study focuses on the finite element modeling of the elastic behavior of plain-woven reinforced WSPC during uniform tensile straining using the ABAQUS software. The data from modelling were compared to the tensile behavior of real WSPC materials. These laminate composites with plain-woven reinforcements were prepared by a two-stage method including (i) powder-coating of woven PA6 textile structure with PA6

microparticles (MP), the latter being previously synthesized via activated anionic ring opening polymerization (AAROP) of ε-caprolactam (ECL) in suspension and (ii) consolidation of the WSPC under optimized pressure and temperature. This production method was denominated as PCCM (powder coating/compression molding). The comparison between the modelled and real stress-strain behavior in tension of these WSPC and the respective textile precursors proves that the selected finite element model was adequate. Based on SEM microscopy with additional image processing and X-ray scattering analyses with the real WSPC samples, the presence of TCL at the matrix-filament interface was postulated and used to modify the matrix/monofilaments interface region in the proposed RVE model. Ultimately, the stress field analysis along the elements of the RVE model was evaluated with the tensile loads applied in warp (0º) or weft (90º) directions.

1. Experimental and test methods

1.1. Materials

The ECL monomer used to obtain the PA6 microparticles was delivered by Brüggemann Chemical (Germany) with reduced moisture content. Before use, it was kept under vacuum for 1 h at 23˚C. Sodium dicaprolactamato-bis-(2-methoxyethoxo)-aluminate (80 wt% in toluene, denominated as DL) selected as polymerization initiator was purchased from Katchem and applied with no further treatment. The polymerization activator was Bruggolen C20P (C20) from Brüggemann Chemical (Germany), which according to the manufacturer data contains 80 wt% of blocked diisocyanate in ECL. All the solvents employed were of "purum" grade obtained from Sigma Aldrich and used as received.

1.2. Plain-woven reinforcements

In the case of reinforcement, plain-woven structures made of air jet textured PA6 continuous filaments (160 dtex) were chosen. The selection of air jet textured filaments essentially causes the introduction of bulkiness into yarns structure followed by the probability of mono-filament's entanglement. In this study, warp and weft filaments were air jet textured with 50 and 100 monofilaments, respectively. The samples were produced in a NFM 6/42 loom and delivered by the Jackob Müller company AG® (Switzerland). To remove contaminations, samples were pre-washed with a non-ionic detergent solution at 30˚C for 30 min and then rinsed with reverse osmosis water for another 15 min. To eliminate any non-chemically bonded hydrophobic finish (oligomers) from the surface of the filament, the reinforcements were immersed in puriss acetone (Sigma-Aldrich) for 30 min and then dried for 120 min at 60˚C. Subsequently, all reinforcements were extended biaxially to 30% of their original

length using a specially designed metal frame and a screen stretching apparatus (Fig. 1). To modify their structural-mechanical properties, the extended reinforcements with the fixed ends were then annealed at 170˚C for 90 min.

Figure 1

The geometrical characteristics of the plain-woven reinforcements and the constitutive filaments, with and without stretching-annealing treatment, are provided in Table 1.

Table 1

1.3.   Preparation of WSPC

The first stage of the WSCP preparation was the solution-precipitation AAROP of ECL using DL as anionic initiator and C20 as activator of ECL to produce PA6 microparticles. The synthesis was described in detail elsewhere [33,34]. In the second stage, the previously extended and annealed woven textile reinforcements were powder coated with calculated amounts of microparticles so that to reach a fiber volume fraction $V_f = 15\%$. To consolidate the WSPC, a Moore hydraulic hot press (United Kingdom) was used with mold dimension of $70 \times 70 \times 2$ mm applying a pressure of 5 MPa during 10 min. The temperature of the compression molding was 215ºC, i.e., above the melting point of the anionic PA6 microparticles and below the one of the PA6 plain-woven textile reinforcement. At the end of process, the molded laminate composites were cooled down to 50˚C at a rate of ca. 40˚C/min. A PA6 neat matrix plate (PN) was produced under the same molding conditions performing the compression molding with PA6microparticles only and used as a reference in the mechanical tests.

1.4.   Matrix/Reinforcements bonding state characterization

To perform 3D geometrical simulation of plain-woven reinforcements, polarized light microscopy (PLM) images of WSPC were obtained after sample microtoming in an Olympus BH-2 light microscope (Japan) equipped with Leica Application Suite 4 software. To measure dimensional parameters of the embedded monofilaments, the PLM images were processed using OpenCV library written in Python. To observe and analyze the bonding state at matrix/reinforcement interface of WSPC, the scanning electron microscopy (SEM) studies were carried out in a Thermo Scientific™ Phenom ProX apparatus (USA). The need for sputter coating in this setup is reduced dramatically resulting in precise dimensional measurements. Direct observation and accurate size

measurement from monofilaments became feasible using Fibermetric (FM) software in combination with the Phenom desktop SEM. To interpret the bonding state at the interface region of the composites, three dimensional images from the surface of embedded monofilaments were generated using 3D Roughness Reconstruction (3DRR) application.

The crystalline structure of plain-woven reinforcements (with and without treatment) and of WSPC was characterized by X-ray diffraction (XRD) performed in a Bruker D8 Discover θ-θ diffractometer working with Cu Kα radiation (λ = 1.541 Å). Linear XRD patterns were collected for all samples in the 2θ range of 5-45˚ with a step time of 2s and step size of 0.1 deg.min^{-1}. A commercial peak-fitting software was used to perform pattern deconvolution by peak fitting as previously indicated by Dencheva et al [35]. The XRD crystallinity index X_c^{XRD} was calculated according to:

$$X_c^{XRD}, \% = \frac{\Sigma U_c}{\Sigma U_c + \Sigma U_a} \tag{1}$$

where ΣU_c and ΣU_a are the integrated areas underneath the respective crystalline peaks and amorphous halo(s), respectively.

1.5.   Mechanical characterization

Plain-woven reinforcements (150×100mm) were tensile tested according to ASTM D 5034 (grab test) using an Instron 4505 testing machine with a standard load cell of 2.5 kN at a crosshead speed of 2 mm.min^{-1}. For the analysis of the tensile properties of plain reinforced WSPC, the normalized test specimens were laser cut from one and the same composite plate and stored for 30 days at 23˚C and 65 % relative humidity before testing. The tensile measurements were performed according to ASTM D 638 in the same testing machine equipped with a standard load cell of 50 kN, at a crosshead speed of 2 mm.min^{-1}, the test sample gauge length being 38 mm. At least five specimens of each sample were tested.

2. Experimental Results

2.1.   Tensile properties of plain-woven reinforcements

Fig. 2 shows the representative stress-strain curves of single plain-woven textile structures used as reinforcements in WSCP, before and after the stretching-annealing treatment in two perpendicular directions. The initial linear zone of the curves in the untreated woven textiles (samples P0, P90) is found between 0-15% relative

deformation, which is due to decrimping and crimp-interchange of the filaments within the textile structure. Increasing the strain, the curve slope increases steeply reaching its peak just before textile failure, which can be attributed to filaments elongation.

Figure 2

The tensile behavior of the woven reinforcements is modified after the stretching-annealing treatment, the respective curves (Fig. 2, P0-A, P90-A) being shifted to the left which corresponds to a smaller initial deformations and higher elastic modulus values. This was expectable that during stretching-annealing treatment, crystallization of PA6 in some of the amorphous domains of the filaments takes place [36]. The tensile properties extracted from the stress-strain curves in Fig. 1 is shown in Table 2. In general, tensile behavior of reinforcements significantly change after stretching-annealing treatment in two principal directions. The elastic modulus of the reinforcements was greater (538%) in the warp (i.e., 0°) than weft (i.e., 90°) directions. However, the treated samples demonstrated identical tensile strength in either direction.

Table 2

2.2. Tensile properties of WSPC

The representative tensile stress-strain curves of warp and weft wise WSPC are illustrated in Fig. 3a, together with the ones of neat anionic PA6 matrix used as reference sample. As shown in Fig. 3a, the tensile behavior of the laminate composites in warp direction (i.e., 0°) shows a nonlinear elastic behavior in the deformational range of $0<\varepsilon<4\%$, followed by a pseudo-plastic plateau up to the breaking point at $\varepsilon = 10\%$. In the case of weft-wise composite (WSPC-90) and PN reference sample, the nonlinear elastic behavior was followed by an abrupt failure at $\varepsilon \approx 5\%$. Generally, Fig. 3a shows that the warp-wise composite displays superior tensile properties as compared to either the weft-vise one or the PN reference.

Considering the identical elongation rate (2 mm.min^{-1}), the tensile stress (MPa)-straining duration(s) curves of the composites and the respective precursors were simultaneously plotted in Fig. 3b. It is shown that the yield point in WSPC-0 and PN reference sample have identical transitional state boundary (vertical interlacing line in Fig. 3b), while the tensile stress-time curve of P(0)-A sample intensely escalated after the initial zone (T_{ε} >60s). These micromechanical deformations can be explained with shear deformation of the longitudinal

7

filaments, extensional deformation of the matrix component and transverse cracking of the filaments [37]. However, the crimp-interchange of the filaments in P(90)-A reinforcement occurs after the yield stress point in stress-time curve of WSPC-90 (Fig. 3b). Thus, the higher tensile strength and stiffness in WSPC-0 samples as compared with the composites reinforced in weft direction can be explained by identical transitional state boundary at the stress-time plots of WSPC-0, PN and P(0)-A (Fig. 3b). However, the transitional state boundary in P(90)-A are situated subsequent of the yield point of PN and WSPC-90 samples.

Figure 3

As seen from Table 3 that displays the most important tensile properties of all WSPC, the use of the P(0)-A reinforcement significantly increased the tensile stiffness of WSPC as compared to either PN reference or to the other WSPC-90 composite – with 45% and 48% respectively. Moreover, warp-wise reinforced WSPC improved the tensile strength with 63% as compared to the composites reinforced in weft direction. Furthermore, embedment of P(0)-A reinforcement resulted in a 174% increase of ductility of WSPC-0 as compared to the WSCP-90 counterpart.

Table 3

3. Structural studies on real WSPC and precursors

3.1. SEM studies

SEM microscopy combined with image processing of neat textile structures and of cryo-fractured WSCP materials was used to determine the thickness of the monofilaments before and after their embedment in the WSPC. The difference between the latter and the former value will render the TCL thickness. Fig. 4a shows the overview SEM images of the plain-woven reinforcements before embedment. A closer visual inspection of the monofilaments is possible in Fig. 4b that provides better magnification for further image processing by blob detection using the FM application of Phenom-world®. As a result, the average thickness of the monofilaments in the PA6 textile structure before embedment was found to be 20.5±0.1 μm (see the histogram inset of Fig. 4c).

Figure 4

The morphology of the PA6 monofilaments embedded into the PA6 matrix was also studied by SEM combined with image processing of the micrographs. The conventional SEM micrograph in Fig. 5a displays a region of cryofractured WSPC. It shows good impregnation of the PA6 monofilaments by the PA6 matrix

material. Moreover, the direct observation of the monofilament/matrix interface shows no sign of melting or surface degradation of the embedded fiber reinforcements. Figs. 5b demonstrate the three-dimensional surface topography of the same region obtained by means of the 3DRR method, whereby in the construction of each 3D image, ten single 2D microscopy images were used. Measuring the thickness of the textile monofilaments after their embedment in the composite matrix produced an average value of 23.5±0.1 µm. Thus, comparing the thickness of original monofilaments and those embedded in the WSPC produces a TCL thickness in the range of 1.0-1.5 µm.

Figure 5

These results were used further in this work to modify the interaction state of monofilaments/matrix components in the proposed RVE model.

3.2. X-ray studies

To reinforce the evidence for the presence of TCL at the matrix/monofilament interface in WSPC, X-ray diffraction studies were performed in which the crystalline microstructure of composites and precursors was studied. Fig. 6 displays representative linear X-ray patterns and their deconvolutions by peak fitting of annealed plain textile reinforcement (6a), anionic PA6 neat matrix (6b) and WSPC (6c). As seen in Fig 6a, the [200] and [002/202] crystalline planes of α-PA6 polymorph with monoclinic unit cell are detected, exhibiting two peaks with 2θ being centered at ca. 20º and 23º [38,39]. Moreover, the [001] and [200] crystalline planes of a pseudo-hexagonal γ-PA6 polymorph with peaks centered between 21 and 22º were also detected. The diffuse scattering of the amorphous PA6 depicted by two wide Gaussian peaks (halos), represented by AM_1 and AM_2. The XRD pattern of annealed plain PA6 textile reinforcement displays symmetric α-PA6 reflections being more intensive and wider than those of the γ-polymorph (Fig. 6a), which is typical of oriented PA6. The neat isotropic anionic PA6 (Fig. 6b), whose crystalline structure is analogous to that of the bulk matrix in WSCP, displays asymmetric and narrower fitted crystalline peaks for α-PA6, as compared with those of the textile reinforcement (Fig. 6a).

Figure 6

As Fig. 6c demonstrates the linear pattern of plain reinforced WSPC and its deconvolution that was made having in mind the results obtained for treated plain-woven reinforcements (Fig. 6a) and PN (Fig. 6b). A separation of the α[200] and α[002/202] reflections of anionic matrix PA6 and the hydrolytic PA6 of the

9

reinforcements was possible here. This turned to be impossible for the respective γ-PA6 reflections (the four peaks denoted with 4 in Fig. 6c). As also shown in Fig. 6c, the α- PA6 peaks of the reinforcements (peaks 5 and 7) are wider and more intense than the α-PA6 peaks of the matrix (peaks 6 and 8). The referred difference is probably due to the orientation of the peaks of the PA6-reinforcements.

Table 4 shows all the data extracted from the deconvolution of the three XRD patterns. The total crystallinity index X_c^{XRD} and the percentage of α- and γ-PA6 polymorphs were calculated according to Eq. (1). The values of the X_c^{XRD} and of the α/γ relation of the stretch-annealed plain-woven textile structure are the highest as compared to those of the neat PN and WSPC. It should be related to the combined mechanical/thermal treatment of the textiles causing additional crystallization predominantly forming the α-PA6 polymorph. Notably, the crystallinity degree and the α/γ relation in the WSPC is exactly between those of PN and P-A. Another interesting result for the WSPC sample is that the α/γ relation of the peaks related to the matrix is close to 1.0, i.e., exactly as in the PN sample, which is pure matrix material - isotropic in terms of orientation anionic PA6. At the same time, the α/γ ratio related with the oriented embedded reinforcements is 2.25, i.e., which is slightly below the value of P-A sample made of oriented hydrolytic PA6 and much higher than that of the fully isotropic anionic PN sample. This experimental fact is in favor of the supposition confirmed by the above SEM studies that the textile monofilaments are coated by a TCL that originates from the matrix PA6 during the WSPC consolidation.

Table 4

In conclusion, the SEM and XRD studies of the WSPC and its precursors support the presence of TCL at the matrix/reinforcement interface. On this basis, each warp or weft filament can be considered as a combination of PA6 originating from the textile monofilaments and PA6 of the TCL domain as depicted schematically in Fig. 7. At the stage of WSPC preparation, the anionic microparticles are selectively molten, leading to good impregnation of all monofilaments (Fig. 7a). Upon solidification of the matrix material, its epitaxial crystallization starts upon every oriented monofilament (Fig. 7b). At the final stages of solidification, it can be assumed that the TCL of the individual monofilaments form a common domain filling all the gaps in the air-jet textured filament (Fig. 7c). Therefore, the RVE of the WSPC of this study can be modeled by implementing three principal elements: PA6 monofilaments (hydrolytic PA6 of the textile structure, oriented), oriented TCL domain from recrystallized anionic PA6 embedding all monofilaments in a certain filament and bulk anionic PA6 matrix between the textile filaments (isotropic).

Figure 7

4. Modeling RVE of WSPC

4.1. 3-D simulation of the RVE

To begin modeling RVE of plain reinforced WSPC, the unit-cell architecture of plain-woven reinforcement was simulated. In general, woven fabrics are produced by the interlacing of two sets of fiber bundles (filaments) such as warp (0°) and weft (90°). The filaments are undulated in the weave structure and the fabric's integrity is preserved by the mechanical interlocking of filaments [40]. The systematic study of woven fabric geometry was launched in 1937 by Peirce [18]. In this model, a two-dimensional unit-cell of plain-woven fabric was built up by superimposing linear and circular yarn segments in which the filaments were assumed to be circular in cross-section and highly incompressible. The Peirce's model is unrealistic due to limitations on the application of this model. Therefore, the inter-filament pressures set up during weaving was considered as flattening of filaments normal to the plane of the fabric in more tightly woven fabrics. Thus, the circular cross section of yarns in fabric structure changed into the elliptical configuration.

Fig. 8a displays selected PLM images of cryo-fractured plain reinforced WSPC with 15 V_{f},% fiber content (3 plies). As shown in Fig. 8a, the embedded filaments in WSPC can be simply illustrated with a rectangular cross-section attached to two semicircular ends. This specific form can be attributed to a transverse dislocation of monofilaments during the WSPC production caused by the so-called "processing loads", i.e., the pressure applied and by the penetration of matrix material (Fig. 8b). In this study, the Kemp model was employed for modeling the plain-woven reinforcement. Network repetition of identical unit-cells in the form of crimp waves and constant filament cross-section in the woven structure as depicted in Fig. 8c was also hypothesized [19]

Figure 8

The equations for Kemp´s model and its derivatives are presented in Equation (2). It should be notified that subscripts i and j represent the warp and weft directions, respectively.

$$\begin{cases} P_i = a_i - b_i + (l'_j - D\theta_j + D \sin\theta_j) \\ l'_j = l_j - a_j + b_j \\ b_i + b_j = D \\ h = 0 \end{cases} \tag{2}$$

Parameter	Description
D	Reinforcement thickness
a	Major diameter of flattened filament

11

b	Minor diameter of flattened filament
p	Average yarn spacing for the fabric as a whole
l	Length of thread axis between planes containing the axes of consecutive cross threads
θ	Maximum angle of filament kernel to the horizontal plane of the reinforcement in radian

As shown in Fig. 8a, one unit-cell from embedded plain-woven reinforcement was magnified and image processed using Canny edge detection algorithm of OpenCV library (Fig. 8d). It functions based on a multi-stage algorithm including noise reduction, image intensity gradient detection, non-maximum suppression and hysteresis thresholding. At the first step, the noise detected in microscopic images were removed with a Gaussian filter and then filtered with a Sobel kernel in both horizontal and vertical directions. This process can enhance finding edge gradient and direction for each pixel. After getting gradient magnitude and direction at every pixel, it checks existence of any unwanted pixels which may not constitute the edge. Subsequently, the elimination of those pixels is performed. At the last stage, two max and min threshold values are defined to discard any edges with intensity gradient more than max value (sure to be edges) and those below min value (sure to be non-edges). As observed through in Fig. 8d, applying compression during molding caused flattering of the filaments, as far as the sum of the crimp heights is equal to the sum of the filaments thickness (i.e., $h = 0$). By capturing ten digitalized microscopic images from cross section of cryofracture surface of the plain reinforced WSPC, and then performing image processing, the geometrical parameters P_i, $a_{i \, or \, j}$, $b_{i \, or \, j}$ were measured and used to calculate the value of θ_j.

In regards to the selected Kemp structural model, the kernel geometry has been drawn and the corresponding cross-section profile lofted using CATIA V5 (Fig. 9). However, to simplify the simulation, the filament cross-section was constantly swept through the kernel geometry and no dimensionally deformation at cross over points was determined. Noticeably, the modeled warp and weft system are comprised of TCL domain and monofilaments which are distributed in equal order in area of the filament´s cross section. Fig. 9 exhibits the final product of the isometric and three side views of simulated annealed plain-woven fabric in which two filaments in warp and weft systems are interlaced with each other.

As Fig. 9 shows, the RVE model of plain reinforced WSPC is divided into several sub-elements, consisting in four intertwined filaments surrounded by the isotropic matrix component. The process began by importing the step files of the composite precursors into the ABAQUS software. There, the assembly operation was executed, as well as the ascription of material properties and boundary conditions. The elastic compliance of the filaments

and the matrix components were assembled to get the effective stiffness of the RVE model. The produced gap between warp and weft filaments in reinforcement unit cell was solid intersected from the box that was overlapped over the reinforcement geometry and then modeled as the matrix component. A surface-based tie constraint was used via ABAQUS to make the translational and rotational motions equal for the surfaces of reinforcements and matrix in RVE model during the simulation. By doing this, each node on the slave surface has the same values for its degrees of freedom as the point on the master surface, providing a perfect interfacial bonding condition (no-slip occurrence) (Fig. 9). Therefore, merely the nodes are tied only where the surfaces are in vicinity to one another. Through the entire models, compatible tetrahedral meshes were applied using the four-node isoparametric tetrahedral element (C3D4) [41]. In this analysis, C3D4 elements were assigned to the proposed FE models due to the relatively low computational time and sufficient possibilities for association between mesh entities and adjacent geometry.

Figure 9

4.2. Material definition

In this study, the elastic properties of PA6 neat matrix and monofilaments were measured experimentally and defined as homogeneous solid continuum elements by using a distribution which includes default values for stiffness (E) and Poisson ratio (v). The warp and weft filaments are air jet textured in which the mechanical properties of the filaments is related to the ones of constituent monofilaments. Hence, the elastic modulus of monofilaments is calculated with respect to the number of monofilaments and elastic modulus of the filaments. Thus, the E-modulus of warp and weft monofilaments were measured, leading to 3.58 and 0.54 GPa, respectively. Notably, it is known that its mechanical properties are independent of matrix and reinforcements [42,43]. Hence, the linear elastic behavior is considered for TCL domain and its E-modulus is determined using a back analysis of experimental results by fitting as better as possible the tensile stress-strain relationship of RVE model with the corresponding experimental data. Five distinct scenarios were applied to model the tensile stiffness of the TCL domain. Table 5 shows the sample designation of the RVE models with respect to the material properties definition. Thus, in the first scenario (M_1), the elastic modulus of TCL (E_{TCL}) was considered identical to the one of the matrix (E_{Matrix}). In scenarios M_2 to M_4 the $\frac{E_{TCL}}{E_{Matrix}}$ ratio has increased gradually. In the last scenario M5, a ration varying between a maximum of $\frac{E_{TCL}}{E_{Matrix}} = 1.3$ and minimum of $\frac{E_{TCL}}{E_{Matrix}} = 1$ was ascribed to the TCL domain

in the warp and weft directions, respectively (M_5).

Table 5

4.3.   Solution technique and Boundary conditions

In this study the displacement-control approach was adopted to undergo the structural analysis of RVE by finite element method. The displacement function was applied using a polynomial expression in which choosing a suitable polynomial function causes better continuity of displacement function within the elements. The effective modulus of elasticity of the composite is determined using the concept of principal virtual work (PVW) which is the work done by a real force acting through a virtual displacement acting through a real displacement. Hence, consider the motion of a deformable body occupying the domain Ω with the boundary Γ in the Euclidean space, subjected to body forces b, external applied traction on boundary Γ_t and displacement boundary conditions $u = \overline{u}$ on Γ_u. In view of the principle of virtual work, the dynamic equilibrium equations and compatibility conditions of an infinitesimal cut of the domain Ω in $\mathbb{R}^3$ can be defined as:

$$\begin{cases} \iiint_{\Omega^{(e)}} \delta\varepsilon^T \sigma d\Omega = \iiint_{\Omega^{(e)}} \delta u^T b d\Omega + \iint_{\Gamma_t^{(e)}} \delta u^T t d\Gamma + [\delta d^{(e)}]^T q^{(e)} \\ \qquad\qquad b = [b_x, b_y, b_z]^T \\ \qquad\qquad t = [t_x, t_y, t_z]^T \end{cases} \tag{3}$$

where $q^{(e)}$ is a matrix of equilibrium nodal forces for the element acting on the virtual nodal displacements $\delta d^{(e)}$ with the following equations,

$$\delta d^{(e)} = \begin{Bmatrix} \delta d_1^{(e)} \\ \delta d_2^{(e)} \\ \delta d_3^{(e)} \end{Bmatrix}, \quad \delta d_i^{(e)} = \begin{Bmatrix} \delta u_i \\ \delta v_i \\ \delta w_i \end{Bmatrix}, \quad q^{(e)} = \begin{Bmatrix} \delta q_1^{(e)} \\ \delta q_2^{(e)} \\ \delta q_3^{(e)} \end{Bmatrix}, \quad q_i^{(e)} = \begin{Bmatrix} F_{xi} \\ F_{yi} \\ F_{zi} \end{Bmatrix} \tag{4}$$

Then, the virtual displacements and the virtual strains are interpolated in terms of the virtual displacement values:

$$\delta u = N\delta d, \quad \delta\varepsilon = B\delta d \tag{5}$$

where the B and N are strain matrices and nodal shape functions, respectively. Substituting the constitutive equation for the stresses (Eqs. 7 and 8) into Eq. 6 gives the equilibrium equation for the element in the standard matrix form after simplification of the virtual displacements is obtained. The four-node isoparametric tetrahedral element (C3D4) were applied entirely in RVE model and PVW relations is expressed by the following equation:

$$\begin{cases} \left(\iiint_{\Omega^{(e)}} B^T D B d\Omega\right) d^{(e)} - \iiint_{\Omega^{(e)}} B^T D \varepsilon^0 d\Omega + \iiint_{\Omega^{(e)}} B^T \sigma^0 d\Omega - \iiint_{\Omega^{(e)}} N^T b d\Omega - \iiint_{\Gamma^{(e)}} N^T t d\Gamma = q^{(e)} \\ \qquad\qquad\qquad\qquad or \\ \qquad\qquad K^{(e)} d^{(e)} - f^{(e)} = q^{(e)} \end{cases} \tag{6}$$

Therefore, the system of equations of structure $Kd=f$ was obtained by assembling the contributions of stiffness matrix ($K^{(e)}$) and equivalent nodal force vector ($f^{(e)}$) for each element. The software allows to get the output of the nodal reaction forces in each component. Due to symmetric geometry of RVE, symmetric boundary conditions are assigned to the nodes on the plane A_1-yz plane (Fig. 9), which have been defined along the x-direction. To simulate uniform strain, a uniform displacement which corresponds to 0.4% strain was smoothly applied using the polynomial expressions to all the nodes lying in the plane A_2 along warp (0º) principal direction, although the other two directions had been constrained (i.e., $y=z=0$). The solution of the model yields a stress state corresponding to the prescribed displacement. The nodal reaction forces on the plane of A_1 model (RVE) was measured. The reaction forces at the prescribed nodes can be computed as follows,

$$R = Kd - f^{\text{external}} \tag{7}$$

where R is the vector of nodal reactions and f^{external} is obtained by assembling the equivalent nodal force vectors $f^{(e)}$ due to external loads only (i.e. excluding the reactions). Indeed, the product Kd can be computed by assembly the element contributions $K^{(e)} d^{(e)}$. The equivalent nodal force vector for each element is calculated by the following equation and then integrated in the global system,

$$f^{(e)} = \iiint_{\Omega^{(e)}} N^T b d\Omega + \iiint_{\Gamma^{(e)}} N^T t d\Gamma + \iiint_{\Omega^{(e)}} B^T D \varepsilon^0 d\Omega - \iiint_{\Omega^{(e)}} B^T \sigma^0 d\Omega \tag{8}$$

In this equation, the first and the second integrals allow taking into account the contribution of the body forces and the surface tractions, respectively, while the last two ones are due to the initial strains and stresses. During the post processing stage, the sum of nodal reaction forces (R) on plane A_1 was divided by that corresponding to the cross-section area, which gives the total stress that is applied on the cross section of RVE model. Eventually, the average stress is divided over the prescribed 0.4 ε,% at that respective direction to calculate the actual stiffness.

5. Discussion
5.1.   Analysis of elastic properties

Fig. 10a shows a comparative study of experimental and numerical stress–strain curve of the WSPC specimen

and proposed RVE models in two principal directions, wherein the average slope of the curve in the strain range 0–0.4% is taken as the E-modulus. As shown in Fig. 10a, considering an identical E-modulus for TCL domain and matrix sub-elements causes significant discrepancies on their linear elastic behavior in either direction. Among all the proposed models, model M4-0 approximate their tensile stress-stain curve in good fashion with the experimental sample in that corresponding direction (WSPC-0). However, assigning $\frac{E_{TCL}}{E_{Matrix}} = 1$ to the proposed model, reproduce the experimental one through weft-wise straining. In case weft-wise WSPC, considering higher elastic moduli of matrix component to the TCL domain leads to the deviation of the RVE stress-strain curve to the one obtained experimentally.

Figure 10

As mentioned in section 1.1, warp and weft filaments contain 50 and 100 monofilaments, respectively, due to determined essential weaving parameter in NFM 6/42 loom. Regarding the same linear density for either filament, the packing density of warp filaments differs to the weft ones. Packing density of a filament results from the distribution of monofilaments through the cross-sections of compact filaments. Existence of higher number of monofilaments in weft filament causes disorder in integration of TCL of monofilaments in air-jet textured filament domain (Fig. 8b). As a conclusion, the different properties of TCL domain in warp and weft filament can be explained by greater area of TCL domain causing better orientation and nucleation of spherulites grow (TCL) in the transversal direction to the nucleating surface (monofilament´s surface). Due to this fact, model M5 in warp and weft directions is created in which the elastic modulus of TCL domain is assigned 30% higher and equal of that in matrix sub-element, respectively (Fig .10b). As one may notice through the analysis of Fig .10b, the numerical results agrees with the experimental ones (i.e., WSPC-0, WSPC-90), while the influence of TCL together with different elastic properties along the warp and weft are considered.

The majority of the researches has been performed concerning the mechanical properties of polyamide monofilaments in the longitudinal direction. In most cases, isotropic elastic properties as well as cylindrical cross sectional structures were assigned to the monofilaments which is indeed inadequate for the analysis of monofilament behavior in complex structures [44–47]. Thus, model 6 (M6) was proposed for further study in which the influence of transverse isotropic mechanical properties on PA6 monofilaments is numerically investigated. However, it would be difficult to characterize the mechanical responses of monofilaments in the

transverse direction due to their extremely small dimensions. Therefore, the monofilaments were assumed to behave linearly elastic, without any plastic deformation in the studied region as for the other sub-elements. Accordingly, a transversely isotropic linear elastic material model was applied to characterize the monofilaments, while the prediction of the mechanical properties had been made to follow the rule of mixture and Chamis's formulae [48]. Stamoulis. et.al [49] studied the transverse mechanical properties of PA6.6 monofilaments with three distinct diameter (120, 230 and 400 μm). Their results depicted higher longitudinal Young's modulus than the one in transverse direction. Therefore, in case of M6-0 and M6-90 models, the mechanical properties in transverse direction (Y and Z axis) of monofilaments were assumed 25% lower than the ones in longitudinal direction (corresponding yarn´s axis). This assumption has been made to observe any significant changes in tensile behavior of RVE model, while anisotropic (M6-0 and M6-90) properties are assigned to the monofilament sub-elements and to compare with M5-0 and M5-90 models. As Fig. 10b shows, minor differences were observed on the stress-strain plots of models 5 and 6. Moreover, giving isotropic mechanical properties to the monofilaments caused better prediction of elastic behavior in WSPC.

5.2. Analysis of stress field corresponding to uniaxial strain

Fig. 11a-c depicts distinctly the distribution of maximum tensile normal (S_{11}), longitudinal shear (S_{12}) and vertical shear (S_{13}) stresses components along deformed RVE model of composites and precursors (M5-0) at 0.4% warp wise (0º) uniform strain (ε). As shown in Fig. 11a, the distribution of S_{11} stress component in a WSPC and sub-elements structure is even along the matrix component. On the other hand, the principal stress, S_{11}, diffused dissimilarly along warp and weft filaments. The negative magnitude of S_{11} in weft filaments is representative of the compressive stresses. Regarding the compressive (in-phase) and extensive (out-phase) behavior of weft and warp filaments, respectively, it is suggested that tensile failure would initiate at interlacing region where the warp and weft monofilaments are crossing over each other (Fig.11a). Moreover, the existence of high S_{11} stress concentration in TCL domain and matrix sub-elements at interlacing area can also cause mechanical failure. The distribution of shear strength (S_{12}, S_{13}) through the composite sub-elements is shown in Fig. 11b and 11c, respectively. Longitudinal straining of WSPC led to the shrinking of the composite precursors transversely because of the negative value of the S_{12} and S_{13}. Nevertheless, the filaments and TCL domain are more contracted than the matrix component. This result can be associated to the global internal forces acting in WSPC, which are elevated by assigning tie constrains to the bonding state of filament/filaments, filament/TCL

17

and TCL/matrix.

Figure 11

Fig. 12a-c presents the distribution of S_{11}, S_{12} and S_{13} stresses components along sub-elements of WSPC, while the tensile strains are applied in weft (90º) direction. Although Fig. 12a shows that the attained S_{22} stress is uniformly distributed along the TCL domain, it unevenly spreads along the matrix and filament domains. Notably, tracing the longitudinal and vertical shear stress in composite sub-elements allows depicting the compressive behavior. However, embedded filaments distributed uniformly the S_{12} and S_{13} stress components as compared with the ones in matrix and TCL domains (Fig. 12b-c). Comparing the stress field analysis in WSPC-0 with WSPC-90, put into evidence that in later, the stresses are distributed more unevenly. Due to this fact one can predict that inconsistent deformation is exerted along the sub-elements when WSPC are submitted to strain in weft direction. Consequently, this caused feeble tensile moduli and strength of WSPC, while they are submitted to loading in that corresponding direction. Fig. 10 allows to observe that the numerical analysis agrees with the experimental data.

Figure 12

6. Conclusion

This paper presents an attempt to understand the influence of transcrystalline layer at matrix/reinforcement interface region through the finite element analysis of plain-woven reinforced PA6-based, single polymer composites (WSPC) in the linear elastic domain. The study presents mechanical, morphological and structural results obtained with composite samples and its precursors that prove the hypothesis of transcrystalline layer (TCL) formation at the matrix/monofilament interface. These data were used to construct an adequate final element model. Based on the performed study, the following conclusions can be drawn:

i. The tensile stiffness and strength of the plain-woven textile reinforcements become greater as a result of the stretching-annealing pretreatment.

ii. The warp-wise (0º) plain reinforced WSPC showed tensile stiffness 45% higher than the one presented by neat anionic matrix and 47% higher than the one obtained along the weft (90º) direction.

iii. A finite element model was presented for a representative volume element (RVE) of WSPC and for the first

time, the effect of TCL has been accounted for in interface region of WSPC. A difference was detected in the areas of the TCL domains both in warp and weft filaments, which led to the considering their elastic moduli as 30% and 0% of the one presented by the matrix sub-element. In doing so, the numerical results reproduced the experimental ones with accuracy.

iv. The analysis of the longitudinal and shear stress fields in the proposed RVE model and its sub-elements showed that the stress components were evenly distributed in the matrix and TCL domain of the WSPC-0 sample. However, S_{22} stress merely distributed along the TCL domain. The negative value of shear strength (S_{12}, S_{13} and S_{23}) along the composite precursors demonstrated transversely dimensional contraction leading compressive behavior.

v. Due to the stress filed analysis, better tensile properties of warp-wise WSPC are predicted as compared with the ones obtained with composites reinforced in weft direction. This is in complete agreement with the experimental mechanical data presented in this study.

Acknowledgements

Data availability statement

The raw/processed data required to reproduce these findings cannot be shared at this time due to legal or ethical reasons.

References

[1]   J. Karger-Kocsis, T. Bárány, Single-polymer composites (SPCs): Status and future trends, Compos. Sci. Technol. 92 (2014) 77–94.

[2]   O.A. Khondker, T. Fukui, M. Inoda, A. Nakai, H. Hamada, Fabrication and mechanical properties of aramid/nylon plain knitted composites, Compos. Part A Appl. Sci. Manuf. 35 (2004) 1195–1205.

[3]   D. Yao, R. Li, P. Nagarajan, Single-polymer composites based on slowly crystallizing polymers, Polym. Eng. Sci. 46 (2006) 1223–1230.

[4]   S.D. Tohidi, A.M. Rocha, N. V Dencheva, A.S. Pouzada, Z. Denchev, Comparative Structural and Mechanical Studies on Polyamide 6 Knitted-Reinforced Single Polymer Composites Prepared by Different Reactive Processing Techniques, Polym. Compos. 40 (2019) 886–897.

[5]   Á. Kmetty, T. Bárány, J. Karger-Kocsis, Self-reinforced polymeric materials: A review, Prog. Polym. Sci. 35 (2010) 1288–1310.

[6]   S. Fakirov, Nano- and Microfibrillar Single-Polymer Composites: A Review, Macromol. Mater. Eng. 298 (2013) 9–32.

[7]   J. Karger-Kocsis, Z. Zhang, Mechanical properties of polymers based on nanostructure and morphology, Struct. Relationships Nanoparticle/Semicrystalline Thermoplast. Compos. Taylor Fr. Abingt. (2005).

[8]   I.M. Ward, P.J. Hine, The science and technology of hot compaction, Polymer (Guildf). 45 (2004) 1413–1427.

[9]   Y. Gong, G. Yang, Single polymer composites by partially melting recycled polyamide 6 fibers: Preparation and characterization, J. Appl. Polym. Sci. 118 (2010) 3357–3363.

[10]   Y. Gong, A. Liu, G. Yang, Polyamide single polymer composites prepared via in situ anionic polymerization of ε-caprolactam, Compos. Part A Appl. Sci. Manuf. 41 (2010) 1006–1011.

[11]   N. Dencheva, Z. Denchev, A.S. Pouzada, A.S. Sampaio, A.M. Rocha, Structure–properties relationship in single polymer composites based on polyamide 6 prepared by in-mold anionic polymerization, J. Mater. Sci. 48 (2013) 7260–7273.

[12]   S.D. Tohidi, A.M. Rocha, N. V Dencheva, Z. Denchev, Microstructural-mechanical properties relationship in single polymer laminate composites based on polyamide 6, Compos. Part B Eng. 153 (2018) 315–324.

[13]   S.D. Tohidi, A.M. Rocha, N. V Dencheva, Z. Denchev, Single polymer laminate composites by compression molding of knitted textiles and microparticles of polyamide 6: Preparation and structure-properties relationship, Compos. Part A Appl. Sci. Manuf. (2018).

[14]   S.D. Tohidi, A.M. Rocha, N. V Dencheva, A.S. Pouzada, Z. Denchev, Comparative Structural and Mechanical Studies on Polyamide 6 Knitted-Reinforced Single Polymer Composites Prepared by Different Reactive Processing Techniques, Polym. Compos. (2018) (in press). doi:10.1002/pc.25075.

[15]   E.J. Barbero, P. Lonetti, K.K. Sikkil, Finite element continuum damage modeling of plain weave reinforced composites, Compos. Part B Eng. 37 (2005) 137–147.

[16]   P. Potluri, V.S. Thammandra, Influence of uniaxial and biaxial tension on meso-scale geometry and strain fields in a woven composite, Compos. Struct. 77 (2007) 405–418.

[17]   Y. Pan, L. Iorga, A.A. Pelegri, Numerical generation of a random chopped fiber composite RVE and its elastic properties, Compos. Sci. Technol. 68 (2008) 2792–2798.

[18]   F.T. Peirce, 5—The geometry of cloth structure, J. Text. Inst. Trans. 28 (1937) 45–96.

[19]   A. Kemp, An extension of Peirce's cloth geometry to the treatment of non-circular threads, J. Text. Inst. (1958) 44–48.

[20]   J.W.S. Hearle, W.J. Shanahan, An energy method for calculations in fabric mechanics part I: Principles of the method, J. Text. Inst. 69 (1978) 81–91.

[21]   J.L. Hu, J.G. Teng, Computational fabric mechanics: Present status and future trends, Finite Elem. Anal. Des. 21 (1996) 225–237.

[22]   G.A. V Leaf, R.D. Anandjiwala, A generalized model of plain woven fabric, Text. Res. J. 55 (1985) 92–99.

[23]   Z. ming Huang, The mechanical properties of composites reinforced with woven and braided fabrics, Compos. Sci. Technol. 60 (2000) 479–498.

[24]   D.M. Blackketter, D.E. Walrath, A.C. Hansen, Modeling damage in a plain weave fabric-reinforced composite material, J. Compos. Technol. Res. 15 (1993) 136–142.

[25]   R.F. Gibson, Principles of composite material mechanics, CRC press, 2016.

[26] C. Gao, L. Yu, H. Liu, L. Chen, Development of self-reinforced polymer composites, Prog. Polym. Sci. 37 (2012) 767–780.

[27] C.-M. Wu, M. Chen, J. Karger-Kocsis, The role of metastability in the micromorphologic features of sheared isotactic polypropylene melts, Polymer (Guildf). 40 (1999) 4195–4203.

[28] D. Rolel, E. Yavin, E. Wachtel, H.D. Wagner, Experimental study of transcrystallinity in UHMWPE/LLDPE composites, Compos. Interfaces. 1 (1993) 225–242.

[29] H. Li, X. Zhang, Y. Duan, D. Wang, L. Li, S. Yan, Influence of crystallization temperature on the morphologies of isotactic polypropylene single-polymer composite, Polymer (Guildf). 45 (2004) 8059–8065.

[30] P.-E. Bourban, N. Bernet, J.-E. Zanetto, J.-A.E. Månson, Material phenomena controlling rapid processing of thermoplastic composites, Compos. Part A Appl. Sci. Manuf. 32 (2001) 1045–1057.

[31] I.P. Orench, F.J. Calleja, P.J. Hine, I.M. Ward, A microindentation study of polyethylene composites produced by hot compaction, J. Appl. Polym. Sci. 100 (2006) 1659–1663.

[32] K. van Rijswijk, H.E.N. Bersee, Reactive processing of textile fiber-reinforced thermoplastic composites – An overview, Compos. Part A Appl. Sci. Manuf. 38 (2007) 666–681.

[33] C. Brêda, N. Dencheva, S. Lanceros-Méndez, Z. Denchev, Preparation and properties of metal-containing polyamide hybrid composites via reactive microencapsulation, J. Mater. Sci. 51 (2016) 10534–10554.

[34] N. Dencheva, Z. Denchev, S. Lanceros-Méndez, T. Ezquerra Sanz, One-Step In Situ Synthesis of Polyamide Microcapsules With Inorganic Payload and Their Transformation into Responsive Thermoplastic Composite Materials, Macromol. Mater. Eng. 301 (2016) 119–124.

[35] N. Dencheva, T. Nunes, M.J. Oliveira, Z. Denchev, Microfibrillar composites based on polyamide/polyethylene blends. 1. Structure investigations in oriented and isotropic polyamide 6, Polymer (Guildf). 46 (2005) 887–901.

[36] J. Hu, Structure and mechanics of woven fabrics, Elsevier, Cambridge, 2004.

[37] T. Ishikawa, T.-W. Chou, One-dimensional micromechanical analysis of woven fabric composites, AIAA J. 21 (1983) 1714–1721.

[38] N. Dencheva, T. Nunes, M.J. Oliveira, Z. Denchev, Microfibrillar composites based on polyamide/polyethylene blends. 1. Structure investigations in oriented and isotropic polyamide 6,

Polymer (Guildf). 46 (2005) 887–901.

[39]   J.M. Samon, J.M. Schultz, B.S. Hsiao, Study of the cold drawing of nylon 6 fiber by in-situ simultaneous small-and wide-angle X-ray scattering techniques, Polymer (Guildf). 41 (2000) 2169–2182.

[40]   X.Q. Peng, J. Cao, A continuum mechanics-based non-orthogonal constitutive model for woven composite fabrics, Compos. Part A Appl. Sci. Manuf. 36 (2005) 859–874.

[41]   O.C. Zienkiewicz, R.L. Taylor, O.C. Zienkiewicz, R.L. Taylor, The finite element method, McGraw-hill London, 1977.

[42]   H. Nuriel, N. Klein, G. Marom, The effect of the transcrystalline layer on the mechanical properties of composite materials in the fibre direction, Compos. Sci. Technol. 59 (1999) 1685–1690.

[43]   H. Brodowsky, E. Mäder, Investigation of Transcrystalline Interphases in Polypropylene/Glass Fiber Composites Using Micromechanical Tests, Fibers. 6 (2018) 16.

[44]   T. Kotani, J. Sweeney, I.M. Ward, The measurement of transverse mechanical properties of polymer fibres, J. Mater. Sci. 29 (1994) 5551–5558.

[45]   M.C.G. Jones, E. Lara-Curzio, A. Kopper, D.C. Martin, The lateral deformation of cross-linkable PPXTA fibres, J. Mater. Sci. 32 (1997) 2855–2871.

[46]   J. Singletary, H. Davis, M.K. Ramasubramanian, W. Knoff, M. Toney, The transverse compression of PPTA fibers Part I Single fiber transverse compression testing, J. Mater. Sci. 35 (2000) 573–581.

[47]   J. Singletary, H. Davis, Y. Song, M.K. Ramasubramanian, W. Knoff, The transverse compression of PPTA fibers Part II Fiber transverse structure, J. Mater. Sci. 35 (2000) 583–592.

[48]   C.C. Chamis, Mechanics of composite materials: past, present, and future, J. Compos. Technol. Res. 11 (1989) 3–14.

[49]   G. Stamoulis, C. Wagner-Kocher, M. Renner, Experimental study of the transverse mechanical properties of polyamide 6.6 monofilaments, J. Mater. Sci. 42 (2007) 4441–4450.

Biaxial stretching aparatus

Plain structure before treatment

Plain structure after treatment

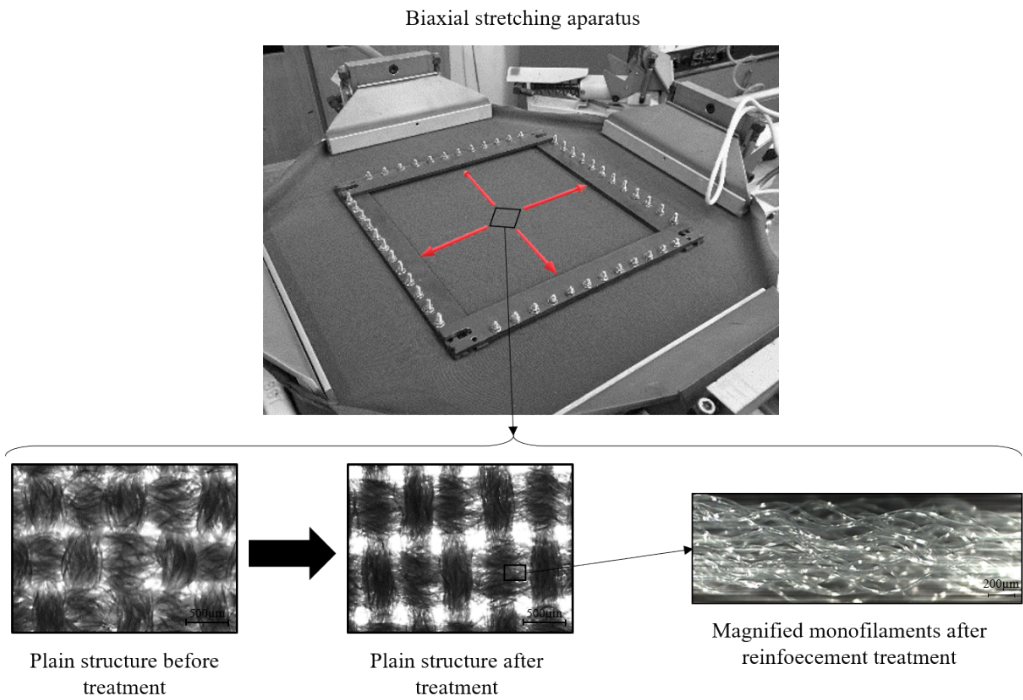Magnified monofilaments after reinfoecement treatment

Fig. 1. Stretching-annealing treatment of the woven reinforcements by combination of adjustable metallic frame and biaxial stretching apparatus. Structural deformation of treated woven structures is visible in the images.
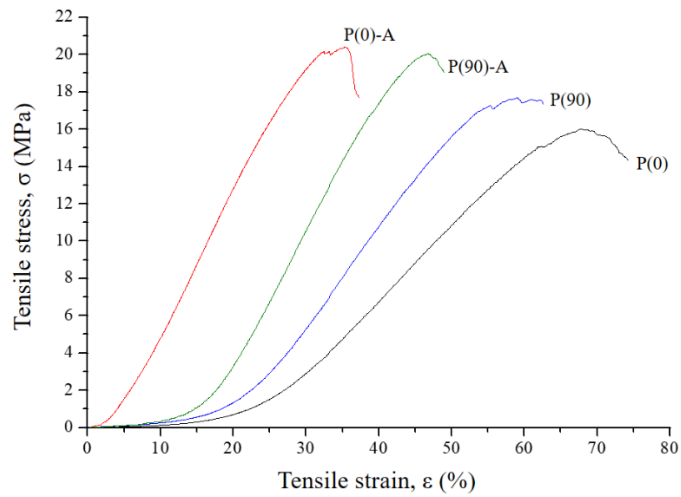

Fig. 2. Representative stress-strain curves of untreated and stretched-annealed plain reinforcements in warp (0º) and weft (90º) directions. The designations are presented in Table 1
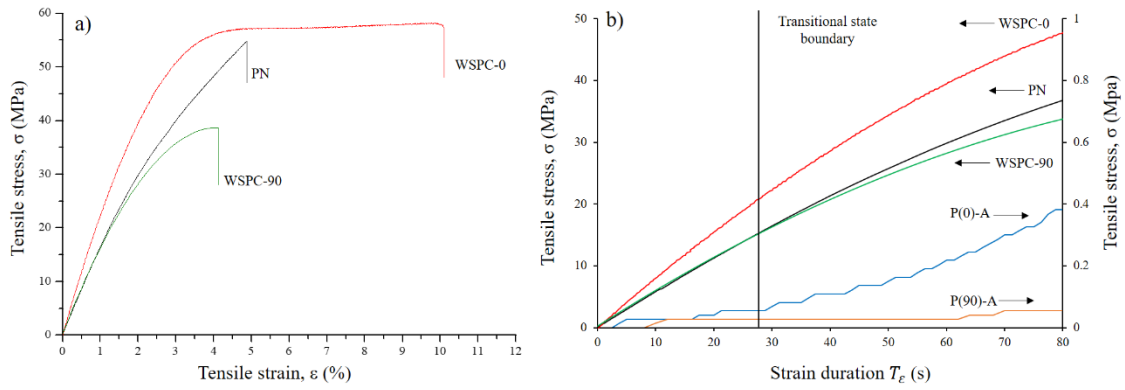
Fig. 3. a) Representative stress-strain curves in tension of P-A reinforced WSPC in two principal directions; The neat anionic matrix PN is presented for reference. b) Simultaneous plotting of tensile stress (MPa)-time (s) curves of laminated composites and precursors.
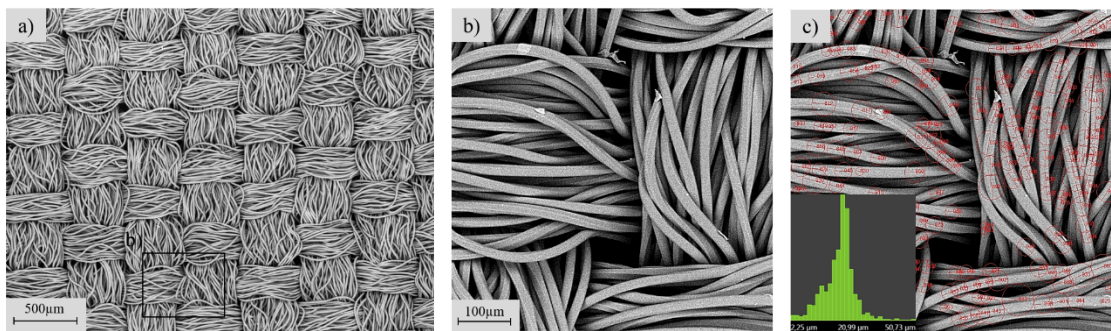

Fig. 4. a) Overview SEM image of stretched-annealed plain structure before lamination; b) Selected magnified SEM image used for image processing; c) Measuring of the embedded monofilament´s thickness completed with blob detection using FM application. The resulting histogram is presented in Fig. 4c.
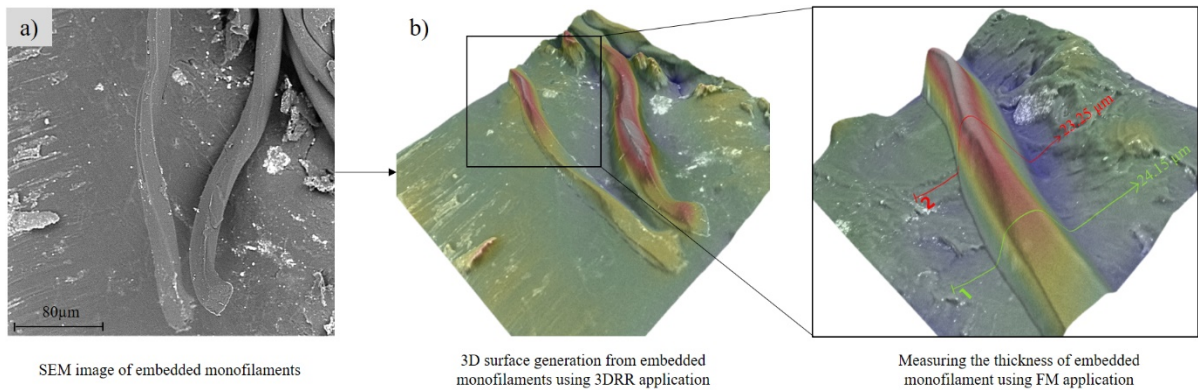
Fig. 5. SEM images of embedded monofilaments after cryofracture of WSPC: a) a single SEM micrograph; b) 3D surface topography of the same area using 3DRR application and thickness measurement of a representative embedded monofilament.
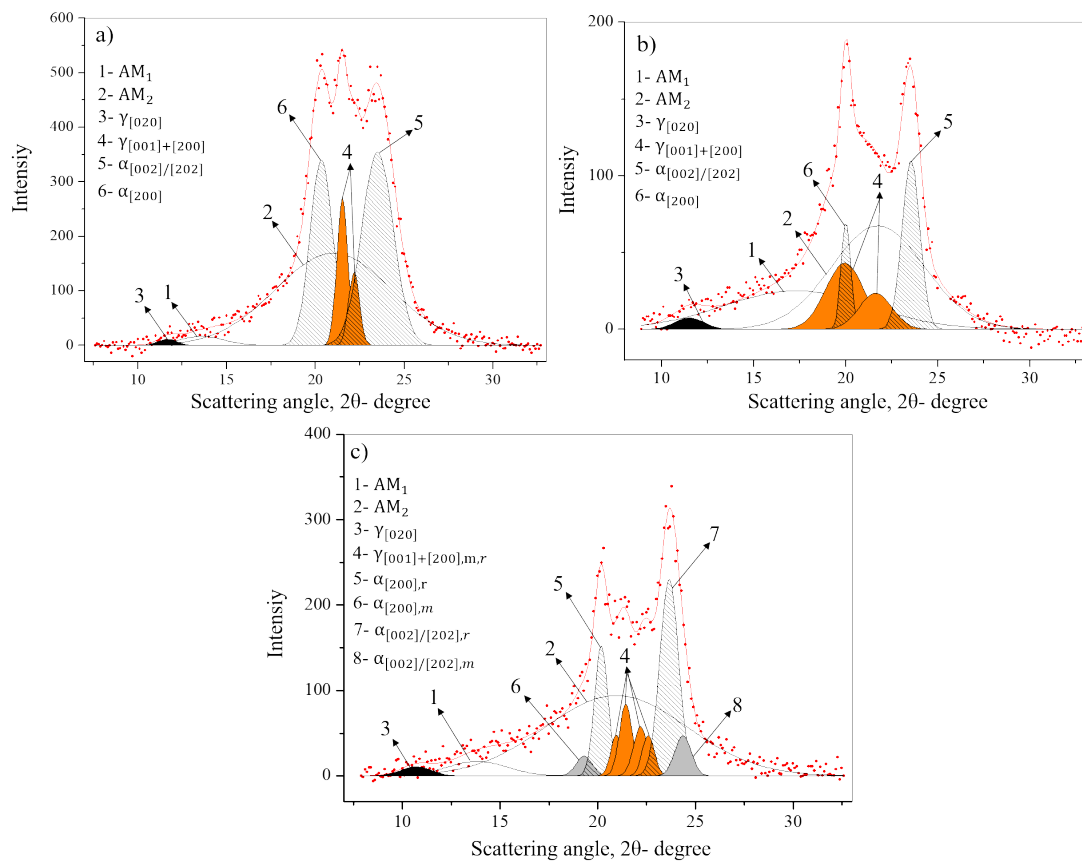

Fig. 6. WAXS patterns and their fits of WSPC building components: a) stretched-annealed plain reinforcement; b) anionic PA6 precursor (PN); c) WSPC. "r" and "m" stand for reinforcement and matrix components, respectively. AM=amorphous portion.
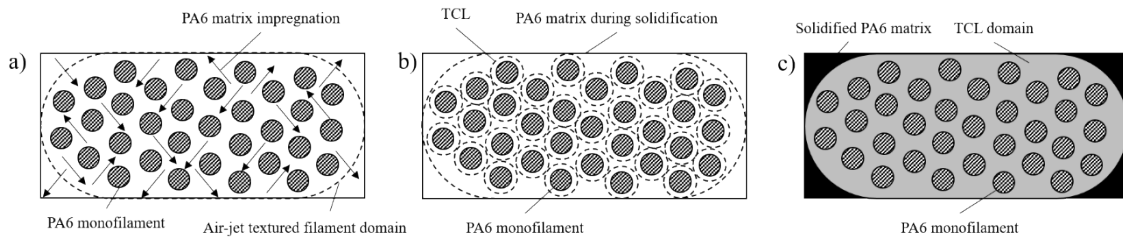
Fig. 7. a) Matrix propagation among monofilaments during compression molding; b) Generation of TCL around each monofilament during solidification procedure; c) Integration of monofilament´s TCL causing the accomplishment of integrity of air-jet textured filament. Changes in: a PA6 matrix impregnation = molten PA6 microparticles.
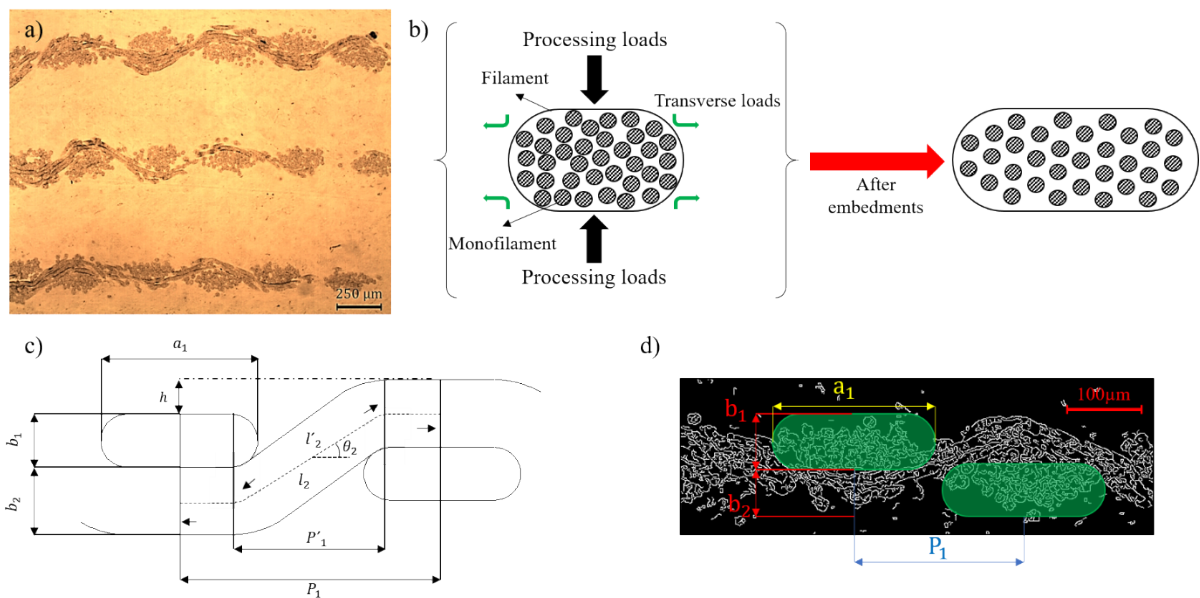

Fig 8. a) PLM image of cryofracture cross section of WSPC and magnification of one unit-cell from embedded plain-woven reinforcement; b) Schematic of transversely dimensional transformation of filaments after embedment; c) Kemp's racetrack section geometry of plain-weave fabrics [19]. d) Image processed using Canny edge detection.
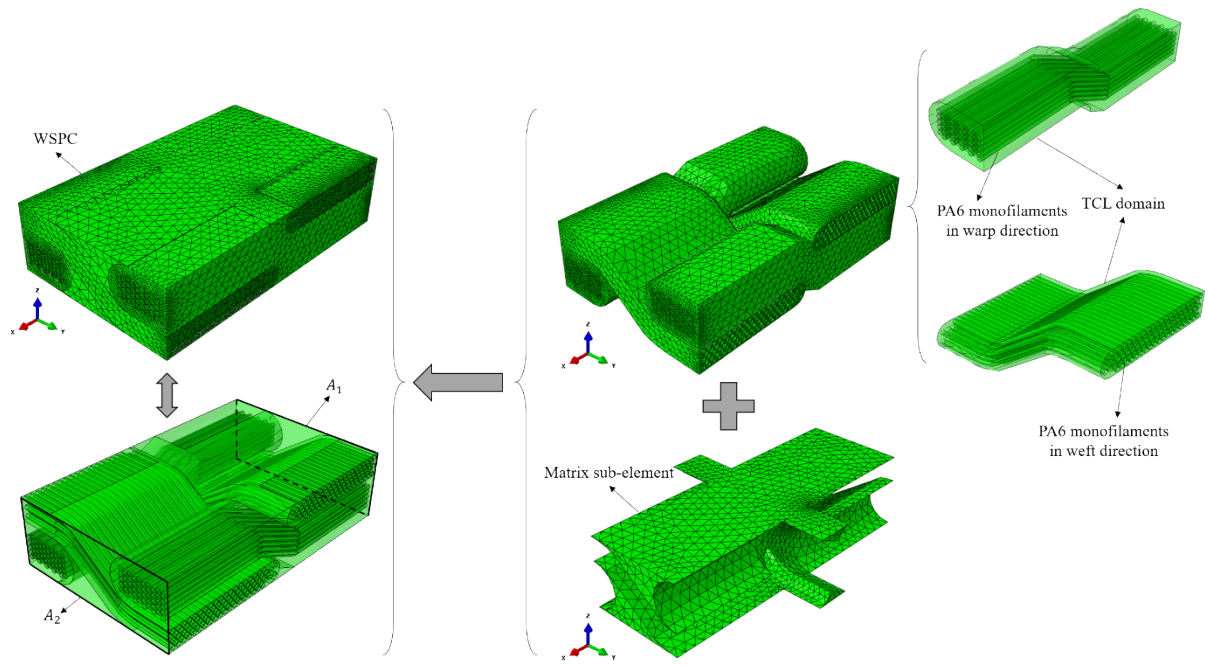
Fig. 9. Simulated 3D model of real size unit-cell of annealed woven reinforcements proposed RVE model of WSPC including monofilaments, TCL domain and matrix components. All sub-elements were mesh generated using the four-node isoparametric tetrahedral element (C3D4).
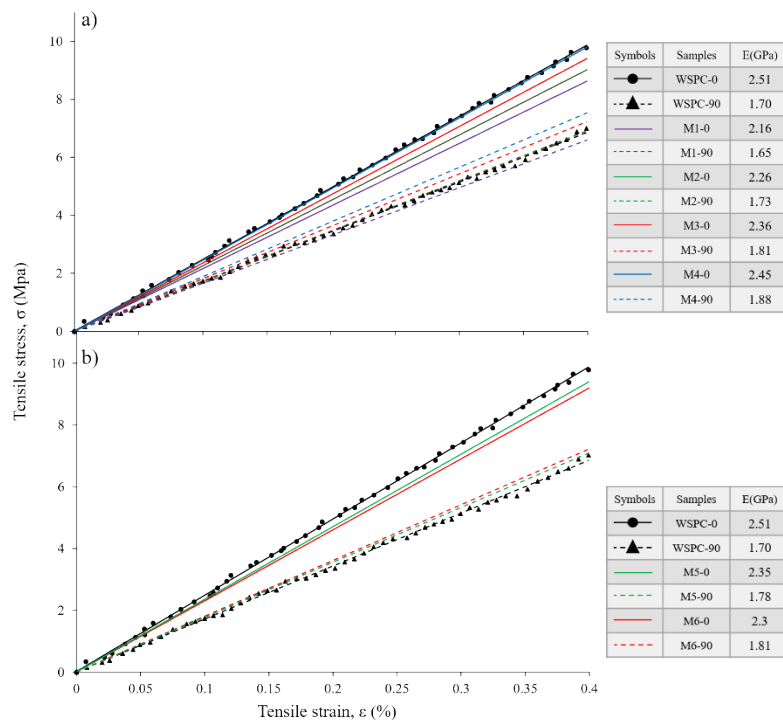
Fig. 10. a) Parametric study of tensile stress-strain curve in experimental and numerical model of WSPC; b) Comparison on stress-strain curves of experimental and M5 and M6 in two principal directions. The measured *E*-modulus of corresponding samples at straining is within the range of 0 to 0.4%. *E* is presented in the inset tables.

Fig. 11. Distribution of a) normal stresses, S11 b) and shear stresses, S12 and c) S13 (in MPa) through WSPC, matrix, TCL domain and monofilament sub-elements of M5-0 RVE model.
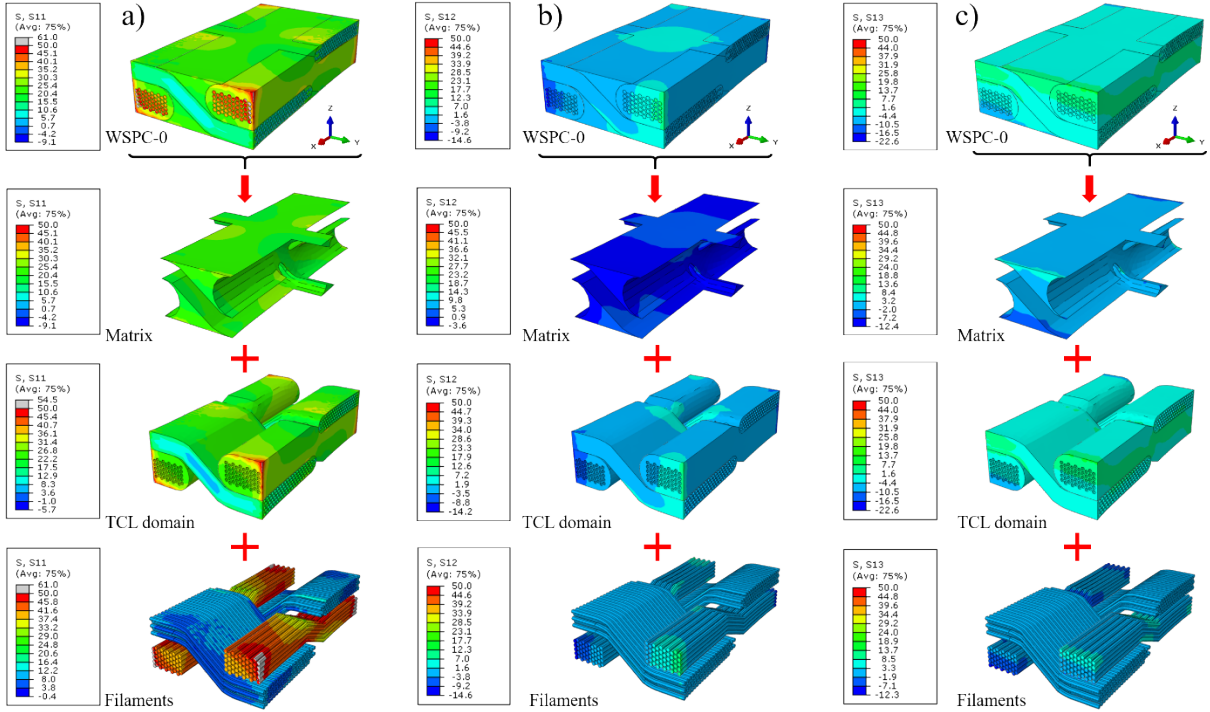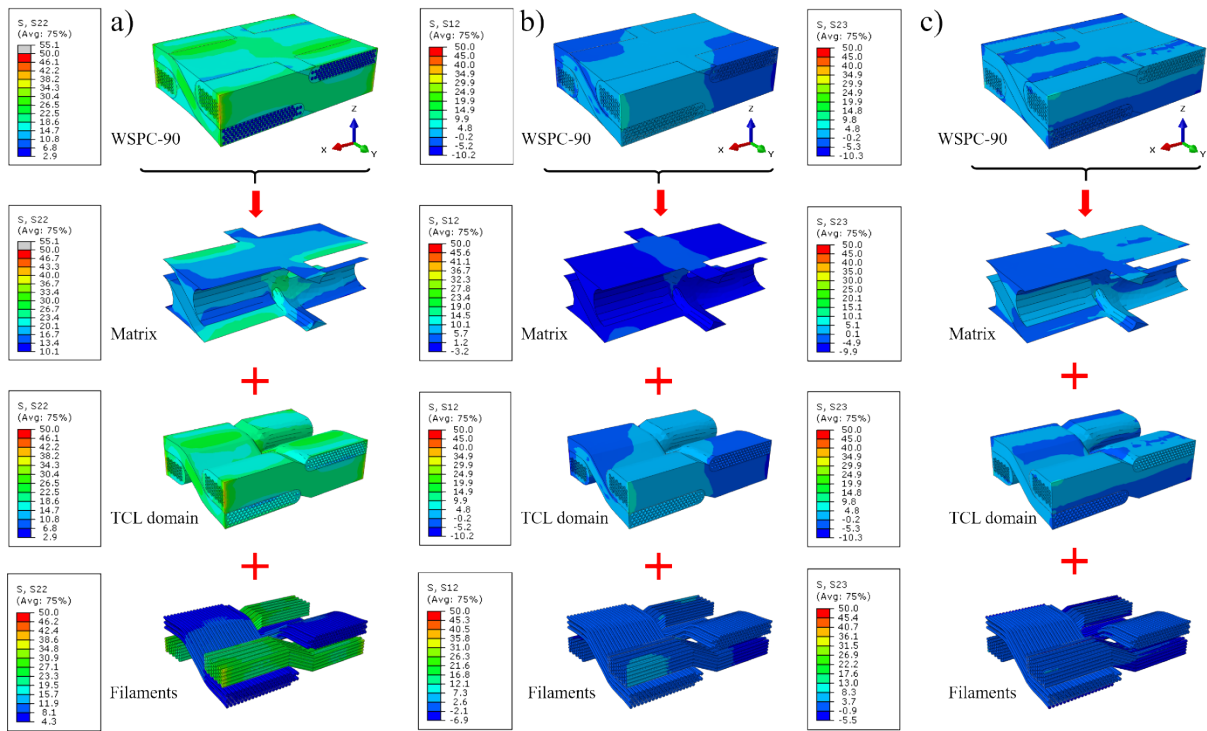
Fig. 12. Distribution of a) normal stresses, S22 b) and shear stresses, S12 and c) S23 (in MPa) through WSPC, matrix, TCL domain and monofilament sub-elements of M5-0 RVE model.

Table 1. Sample designation and properties of plain-woven reinforcements

Type	Treatment	Designation	Density[a]	Areal weight (g.m^{-2})	Thickness (mm)
Plain	No	P(0 or 90[b])	22×16	147.6±1.7	0.58±0.01
	Yes	P(0 or 90[b])-A	20×12	111.0±2.1	0.42±0.01

[a] Density=Warp filaments.cm^{-1} × Weft filaments.cm^{-1}

[b] 0 and 90 stand for warp and weft direction, respectively.

Table 2. Tensile properties of the woven reinforcements before and after treatment.

Specimens	Tensile Stiffness E (MPa)	Tensile Strength σ_{max} (MPa)	Strain at rupture ε_{break} (%)
P(0)	0.8 ± 0.1	15.4 ± 0.8	67.2 ± 0.7
P(90)	2.2 ± 0.2	17.4 ± 0.4	61.1 ± 1.8
P(0)-A	21.7 ± 1.1	19.4 ± 1.0	28.1 ± 1.0
P(90)-A	3.4 ± 0.3	19.0 ± 1.0	46.2 ± 1.4

Table 3. Tensile properties of WSPC comprising elastic modulus E, tensile strength σ_{max}, tensile stress at break (σ_{break}) and strain at break ε_{break}.

Specimens	E (GPa)	σ_{max}(MPa)	σ_{break} (MPa)	ε_{break} (%)
PN	1.73 ± 0.02	56.7 ± 1.8	56.7 ± 1.8	5.2 ± 0.1
WSPC-0	2.51 ± 0.03	61.7 ± 1.0	55.7 ± 1.6	10.7 ± 0.6
WSPC-90	1.70 ± 0.06	37.9 ± 0.8	37.9 ± 0.8	3.9 ± 0.3

Table 4. Data from the deconvolution of the XRD patterns of WSPC, textile structures and anionic PA6 precursors

Sample	$\alpha\%$	$\gamma\ \%$	$X_c^{XRD},\%$	$\dfrac{\alpha}{\gamma}$
PN	17.4	17.5	34.9	1.00
P-A	43.12	10.66	53.78	4.05
WSPC-0	25.27^R 4.59^M $\mathbf{29.86^T}$	8.81^R 4.46^M $\mathbf{13.27^T}$	43.13	2.25

Note: R, M and T stand for reinforcement, matrix division and total values, respectively.

Table 5. Sample designation of the RVE models in relation with the material properties definition

RVE designations	Direction	Elastic properties rario *	$E_{TCL\ domain}$ (GPa)	E_{Matrix} (GPa)	$E_{Monofilaments}$ (GPa)
M1	Warp and Weft	$\dfrac{E_{\text{TCL domain}}}{E_{\text{matrix}}}=1$	1.73		
M2	Warp and Weft	$\dfrac{E_{\text{TCL domain}}}{E_{\text{matrix}}}=1.1$	1.90	1.73	Warp: 3.58 Weft: 0.54
M3	Warp and Weft	$\dfrac{E_{\text{TCL domain}}}{E_{\text{matrix}}}=1.2$	2.07		
M4	Warp and Weft	$\dfrac{E_{\text{TCL domain}}}{E_{\text{matrix}}}=1.3$	2.25		
M5	Warp	$\dfrac{E_{\text{TCL domain}}}{E_{\text{matrix}}}=1.3$	2.25	1.73	Warp: 3.58 Weft: 0.54
	Weft	$\dfrac{E_{\text{TCL domain}}}{E_{\text{matrix}}}=1$	1.73		

Note: E stands for the elastic modulus.